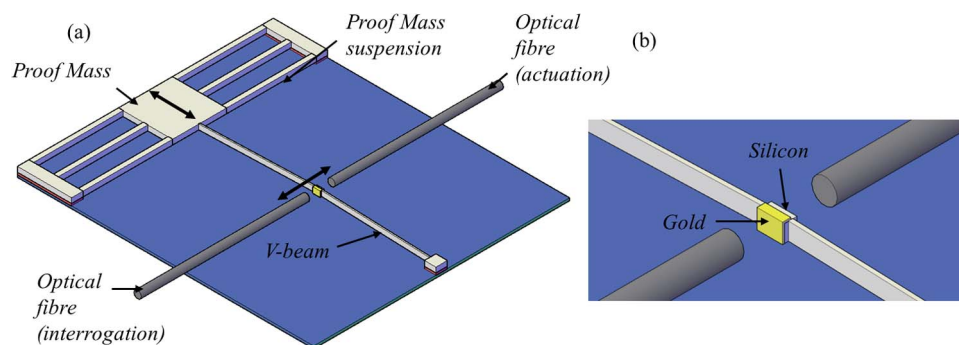


# Remote Photothermal Actuation for Calibration of In-Phase and Quadrature Readout in a Mechanically Amplified Fabry–Pérot Accelerometer

Volume 6, Number 3, June 2014

E. Davies  
D. S. George  
A. S. Holmes



DOI: 10.1109/JPHOT.2014.2326652  
1943-0655 © 2014 IEEE

# Remote Photothermal Actuation for Calibration of In-Phase and Quadrature Readout in a Mechanically Amplified Fabry–Pérot Accelerometer

E. Davies,<sup>1</sup> D. S. George,<sup>2</sup> and A. S. Holmes<sup>1</sup>

<sup>1</sup>Department of Electrical and Electronic Engineering (EEE), Imperial College London, London SW7 2AZ, U.K.

<sup>2</sup>Atomic Weapons Establishment (AWE) PLC, Berkshire RG7 4PR, U.K.

DOI: 10.1109/JPHOT.2014.2326652

*This work is licensed under a Creative Commons Attribution 3.0 License. For more information, see <http://creativecommons.org/licenses/by/3.0/>*

Manuscript received February 27, 2014; revised April 29, 2014; accepted May 10, 2014. Date of publication May 30, 2014; date of current version June 6, 2014. This work was supported by AWE plc. Corresponding author: E. Davies.

**Abstract:** A mechanically amplified Fabry–Pérot optical accelerometer is reported in which photothermal actuation is used to calibrate the in-phase and quadrature (I&Q) readout. The Fabry–Pérot interferometer (FPI) is formed between a gold-coated silicon mirror, situated in the middle of a V-beam amplifier, and the end surface of a cleaved optical fiber. On the opposite side of the silicon mirror, a further cleaved optical fiber transmits near-infrared laser light ( $\lambda = 785$  nm), which is absorbed by the uncoated silicon causing heating. The thermal expansion of the V-beam is translated into an amplified change in cavity length of the FPI, large enough for the  $2\pi$ -phase variation necessary for I&Q calibration. A simple 1D thermal analysis of the structure has been developed to predict the relationship between laser power and change in cavity length. A device having a V-beam of length 1.8 mm, width 20  $\mu\text{m}$ , and angle  $2^\circ$  was found to undergo a cavity length change of 785 nm at 30 mW input power. The device response was approximately linear for input accelerations from 0.01 to 15 g. The noise was measured to be  $\sim 60 \mu\text{g}/\sqrt{\text{Hz}}$  from 100 Hz to 3.0 kHz, whereas the limit of detection was 47.7 mg from dc to 3.0 kHz.

**Index Terms:** Micro-optics, sensors, lasers, MEMS, optical devices, thermal actuation and Fabry–Pérot.

## 1. Introduction

Optical accelerometers are attractive due to their high sensitivity, immunity to electromagnetic radiation and employability in harsh environments. Typically such devices employ a proof mass supported on an elastic suspension inside a housing. Under applied acceleration, inertial forces cause the proof mass to be displaced relative to the housing and this displacement is measured by a transducer. Various optical transducers have been studied for measuring the proof mass displacement, including optical fiber Bragg gratings [1], [2], shutters/intensity modulators [3], [4] and Fabry–Pérot interferometers (FPIs) [5]. FPI devices based on MEMS (micro electro mechanical systems) technology are particularly attractive because they have the potential for higher sensitivity than intensity-based devices while being compatible with microfabrication [6]–[8]. The result is a device which is ultimately limited in size only by the micromachining techniques

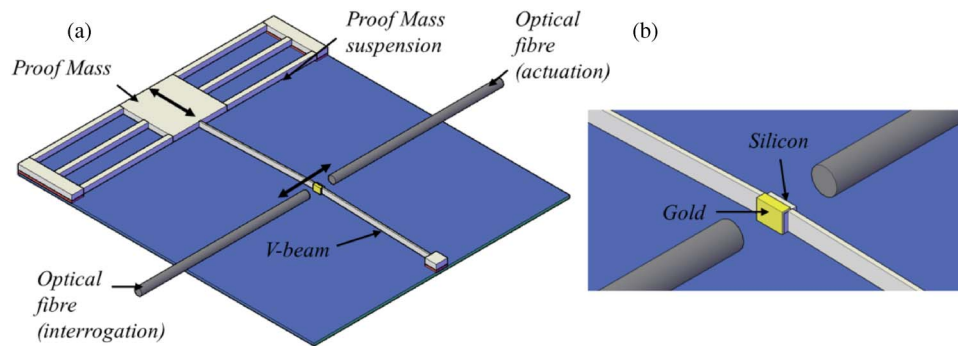


Fig. 1. (a) Schematic of the V-beam amplified accelerometer. (b) Close-up view showing FPI cavity formed between optical fiber and gold-coated silicon mirror and second optical fiber delivering laser light for photothermal actuation to opposite (uncoated) side of mirror block.

employed and which allows for a large degree of control over the proof mass dimensions and the spring constant.

There is an inherent trade-off between bandwidth and sensitivity which is fundamental to all accelerometers employing a suspended proof mass. The steady state proof mass deflection,  $\Delta x$ , under a constant applied acceleration,  $a$ , is given by  $\Delta x = ma/k$  where  $m$  is the proof mass and  $k$  is the stiffness of the elastic suspension. This can be re-written in terms of the mechanical resonant frequency  $\omega_0 = \sqrt{(k/m)}$  of the mass-spring system to give

$$\Delta x = a/\omega_0^2. \quad (1)$$

In an FPI-based device the sensitivity can be improved by increasing the finesse of the transducer cavity. However, on the micro-scale this adds further complications in production. An alternative is to amplify the motion of the proof mass allowing high resonant frequencies to be combined with large displacements at the transducer input. Mechanical amplification using lever mechanisms has been demonstrated previously in accelerometers with both optical [9] and capacitive [10] readout.

Amplifying the displacement of the proof mass often leads to a change in cavity length sufficient to produce a variation in round-trip phase shift greater than  $2\pi$ . In this case an FPI interrogation technique capable of operating over multiple fringes must be employed, such as in-phase and quadrature (I&Q). This technique has a rapid response, making it the preferred approach for many applications [7], [11]. It is also compatible with low-finesse cavities where the FPI spectrum is roughly sinusoidal in shape [12]. The cavity is interrogated simultaneously at two wavelengths,  $\lambda_1$  and  $\lambda_2$ , chosen to produce round-trip phase shifts separated by  $90^\circ$ . The cavity length variations induced by acceleration can then be estimated from the returned intensities at the different wavelengths [13]–[15]. For effective deployment of accelerometers using I&Q interrogation, the devices typically have to be calibrated or normalized before use, in order to remove the effects of offset and gain errors [14]. This is usually achieved by shaking the devices vigorously to produce a  $\geq 2\pi$  change in phase, although T. Požar and J. Možina have investigated algorithms to relax this requirement by estimating the full shape of the Lissajous figure formed by the transducer outputs based on only a partial measurement [16].

In this paper, we demonstrate the use of remote photothermal actuation for calibration of a mechanically amplified FPI optical accelerometer with I&Q readout. This work extends our earlier investigation of mechanical amplification in optical accelerometers using V-beam structures, as reported in [17], [18]. A schematic of the device investigated in the present work is shown in Fig. 1. The Fabry-Pérot cavity, which is used to measure changes in acceleration, is formed between a cleaved optical fiber, acting as both the input and output mirror, and a gold coated silicon mirror block located at the mid-point of the V-beam. The interrogation wavelength is

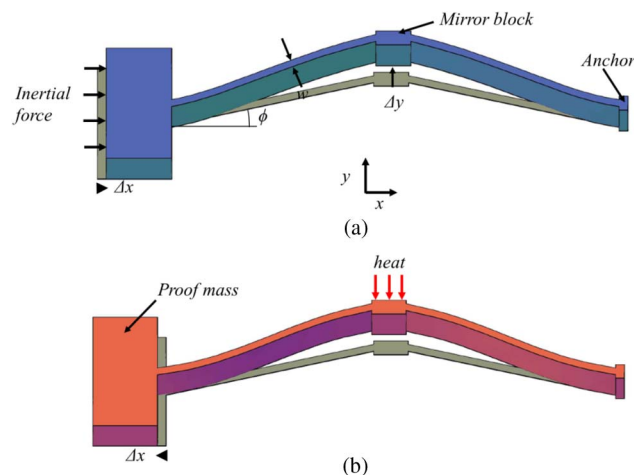


Fig. 2. Structure of the V-beam amplifier showing (a) mechanical amplification with the proof mass moving in the positive  $x$ -direction under an applied inertial force and (b) photothermal actuation with the induced heating causing proof mass displacement in the negative  $x$ -direction. In each diagram, the shadow shows the original position of the V-beam (before application of force/heat).

1.55  $\mu\text{m}$ , in the short-wavelength infrared. A second optical fiber, located on the opposite side of the silicon block, is used to deliver near-infrared (NIR) light (785 nm wavelength) for photothermal actuation of the V-beam. This side of the silicon block is uncoated to allow effective absorption in the NIR. Additional structures for locating the optical fibers are omitted from Fig. 1 for simplicity.

The use of photothermal actuation in MEMS devices is not new. For example, Zhang *et al.* [19] and Churenkov [20] used photothermal actuation to investigate the mechanical properties of silicon micro-resonators by modulating the light source at the resonance frequency of the structures. Laser-driven asymmetrical thermal actuators have also been developed and investigated by Ma *et al.* [21] and Liu *et al.* [22]; however these devices were not used for specific applications. Another area of interest is the use of light to power automated robots. The idea of using V-beams for such applications was introduced by Szabo and Kladitis [23] and taken further with the production of an actual micro-robot by Pac *et al.* [24]. The advantage of using photothermal actuation in the present work is that it allows remote calibration without the need for electrical signals.

The remainder of this paper is organized as follows. In Section 2 a description is given of the operating principles of the V-beam amplifier and simple expressions are derived to describe the structure's mechanical and thermal properties. The I&Q operating principle is then outlined including a discussion on the chosen device design. Section 3 summarizes the fabrication of the accelerometer in conjunction with the methodology used to interrogate the device's response to varying laser power and accelerations. Section 4 presents the results achieved and provides comparisons with the theoretical predictions of the performance. Conclusions are contained in Section 5.

## 2. Theory of Operation and Device Design

### 2.1. Mechanical and Thermal Amplification

The principle governing the mechanical amplification via a V-beam can be understood with the aid of Fig. 2(a), where the V-beam angle  $\phi$  has been exaggerated for illustration. Under an applied acceleration, the displacement  $\Delta x$  of the proof mass in the  $x$ -direction causes a compression of the structure along the  $x$ -axis. To accommodate this, the V-beam deflects laterally, resulting in an amplified displacement  $\Delta y$  at the mirror block. Provided the displacements are small, as they will be in an FPI device, the structure can be assumed to exhibit linear elastic behavior. In this case,

with reference to Fig. 2(a), the mechanical amplification factor of the V-beam can readily be shown to be [18]

$$m = \frac{\Delta y}{\Delta x} = \frac{(1 - \alpha)}{2(u + \alpha/u)} \quad (2)$$

where  $u = \tan\phi$  and  $\alpha = (w/l)^2$ , with  $w$  and  $l$  being the width and length of the V-beam flexures, respectively.

The behavior of the structure under photothermal actuation is shown in Fig. 2(b). In this case the V-beam undergoes frustrated thermal expansion, causing the proof mass to move in the negative  $x$ -direction i.e., away from the V-beam anchor. Equilibrium is reached when the elastic forces due to the proof mass suspension and the V-beam are balanced, so the resulting displacement  $\Delta x$  of the proof mass satisfies

$$k_v(\Delta L - \Delta x) = k_{spr}\Delta x \quad (3)$$

where  $k_v$  is the spring constant of the V-beam,  $k_{spr}$  is the spring constant of the proof mass suspension, and  $\Delta L$  is the change in length (along the  $x$ -axis) that would occur in the V-beam if its thermal expansion were unconstrained. The compression  $(\Delta L - \Delta x)$  of the heated V-beam leads to an amplified displacement at the mirror block of  $\Delta y = m(\Delta L - \Delta x)$ . Eliminating  $\Delta x$  from this expression with the aid of eq. (3) gives

$$\Delta y = m_{th}\Delta L; \quad m_{th} = m \frac{k_{spr}}{k_{spr} + k_v} \quad (4)$$

where  $m_{th}$  is the *thermal amplification factor*, defined as the ratio of the mirror displacement to the unconstrained thermal expansion of the V-beam. From eq. (4) we see that  $m_{th}$  is lower than the mechanical amplification factor by an amount which depends on the relative magnitudes of the spring constants. To take full advantage of the properties of the V-beam, and have efficient thermal actuation, it is required that  $k_{spr} \gg k_v$ .

## 2.2. Thermal Modeling

In this section a one-dimensional thermal model is developed to assess the theoretical performance of the device under photothermal actuation. In addition to thermal conduction in the silicon structure, the model includes air-mediated conductive losses to adjacent silicon features and the underlying substrate. However, radiative losses, which become significant at higher temperatures [25], are neglected because the temperature rises are expected to be relatively low. Assuming steady-state, the one-dimensional heat flow equation for the V-beam structure can be written as

$$k_s A \frac{d^2 T}{dx^2} + qA - (2h_s t + h_b w)(T - T_0) = 0 \quad (5)$$

where  $k_s$  is the thermal conductivity of the silicon,  $w$  is the width of the beam,  $t$  is the depth of the beam,  $A = wt$  is the beam cross-section,  $T$  is the local temperature,  $qA$  is the local input power per unit length due to heating by the laser ( $q$  being the power input per unit volume, averaged over the cross-section), and  $T_0$  is the temperature of the substrate (which is assumed to be a perfect heat sink). The coefficients  $h_s = k_a/d_s$  and  $h_b = k_a/d_b$  represent the conductive heat losses from the side wall and lower surface of the V-beam, respectively, where  $k_a$  is the thermal conductivity of air, and  $d_s$  and  $d_b$  are the associated air gaps. Due to the way the device is fabricated, by deep reacting ion etching of the device layer in a bonded silicon-on-insulator (BSOI) wafer, the V-beam has adjacent bulk silicon on both sides and also beneath it, and so conductive losses across the associated air-gaps must be taken into account. However, there is no capping

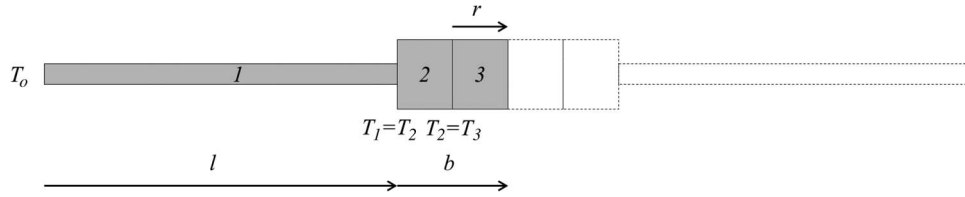


Fig. 3. One-dimensional thermal model of the V-beam, with only one half being considered due to symmetry. Section 1 represents a single arm of the V-beam, while Sections 2 and 3 combined represent one half of the central silicon mirror block.

layer above the structure, so losses from the top surface will be small and are neglected in this analysis. Setting

$$\beta = \frac{q}{k_s}, \quad \gamma = \sqrt{\frac{h}{k_s A}} \text{ and } h = 2h_s t + h_b w \quad (6)$$

the solution to eq. (5) in regions of constant  $q$  is

$$T(x) = C_1 e^{\gamma x} + C_2 e^{-\gamma x} + \varepsilon \quad (7)$$

where the coefficients  $C_1$  and  $C_2$  are determined from the boundary conditions, and

$$\varepsilon = \frac{\beta + \gamma^2 T_o}{\gamma^2} = \frac{qA}{h} + T_o. \quad (8)$$

Due to the symmetry of the problem, only one half of the V-beam needs to be modeled in order to calculate the temperature distribution along the entire structure. As shown in Fig. 3, the half-structure to be modeled is divided into three sections, one representing the V-beam arm, and the other two making up one side of the mirror block. The laser heating is assumed to occur only in Section 3, and by varying the relative sizes of Sections 2 and 3 (by means of the parameter  $r$ ) the effect of varying the spot size of the heating laser can be investigated.

Assuming the heating laser beam impinges only on Section 3, the power input per unit volume in this section is taken to be

$$q_3 = \frac{(1 - R)P_o}{2A_3 r} \quad (9)$$

where  $R$  is the reflection coefficient at the air-silicon interface and  $P_o$  is the total power of the incident laser beam. Eq. (9) assumes that all of the NIR laser energy entering the silicon mirror block is absorbed, which is reasonable given that the mirror block is  $60 \mu\text{m}$  wide and the absorption length of  $785 \text{ nm}$  wavelength light in silicon is  $\sim 8.9 \mu\text{m}$ . The factor of  $1/2$  is included to account for only half of the V-beam being analyzed. Since the laser beam is confined to Section 3, there is no heating in the other sections, and accordingly it is assumed that  $q_1 = q_2 = 0$ .

Further to the boundary conditions shown in Fig. 3, which represent continuity of temperature at the boundaries between sections, the heat flux must also be continuous at these interfaces, leading to

$$-k_s A_1 \frac{dT_1(l)}{dx} = -k_s A_2 \frac{dT_2(l)}{dx}, \quad -k_s A_2 \frac{dT_2(l+b-r)}{dx} = -k_s A_3 \frac{dT_3(l+b-r)}{dx} \quad \text{and} \quad \frac{dT_3(l+b)}{dx} = 0 \quad (10)$$

TABLE 1

Parameters used to model the V beam behavior under photothermal actuation

Name	Description	Value
$k_a$	Thermal conductivity of air	$2.6 \times 10^{-2} \text{ Wm}^{-1}\text{K}^{-1}$
$k_s$	Thermal conductivity of silicon	$130 \text{ Wm}^{-1}\text{K}^{-1}$
$d_s$	Gap between V-beam and adjacent silicon	$10 \text{ }\mu\text{m}$
$d_b$	Gap between V-beam and underlying substrate	$10 \text{ }\mu\text{m}$
$\chi$	Silicon linear coefficient of thermal expansion	$2.7 \times 10^{-6} \text{ K}^{-1}$
$l$	V-beam length	$1.8 \text{ mm}$
$w$	V-beam width	$20 \text{ }\mu\text{m}$
$t$	V-beam and silicon mirror block depth	$79 \text{ }\mu\text{m}$
$b$	Half mirror block length	$62.5 \text{ }\mu\text{m}$
$T_0$	Substrate temperature	$293 \text{ K}$
$m_{th}$	Thermal amplification	$7.4$
$r$	Width of section illuminated by NIR laser	$10 \text{ }\mu\text{m}$
$R$	Reflection coefficient of silicon at $\lambda = 785 \text{ nm}$	$0.33$

where  $b$  is half the width of the silicon mirror block. Assuming solutions of the form in eq. (7) in each section, application of the above boundary conditions leads to the matrix equation for the coefficients

$$\begin{bmatrix}
 1 & 1 & 0 & 0 & 0 & 0 \\
 e^{\gamma_1 l} & e^{-\gamma_1 l} & -e^{\gamma_2 l} & -e^{-\gamma_2 l} & 0 & 0 \\
 A_1 \gamma_1 e^{\gamma_1 l} & -A_1 \gamma_1 e^{-\gamma_1 l} & -A_2 \gamma_2 e^{\gamma_2 l} & A_2 \gamma_2 e^{-\gamma_2 l} & 0 & 0 \\
 0 & 0 & e^{\gamma_2(l+b-r)} & e^{-\gamma_2(l+b-r)} & -e^{\gamma_3(l+b-r)} & -e^{\gamma_3(l+b-r)} \\
 0 & 0 & A_2 \gamma_2 e^{\gamma_2(l+b-r)} & -A_2 \gamma_2 e^{-\gamma_2(l+b-r)} & -A_3 \gamma_3 e^{\gamma_3(l+b-r)} & A_3 \gamma_3 e^{-\gamma_3(l+b-r)} \\
 0 & 0 & 0 & 0 & e^{\gamma_3(l+b)} & -e^{-\gamma_3(l+b)}
 \end{bmatrix}
 \times
 \begin{bmatrix}
 C_{11} \\
 C_{12} \\
 C_{21} \\
 C_{22} \\
 C_{31} \\
 C_{32}
 \end{bmatrix}
 =
 \begin{bmatrix}
 T_0 - \varepsilon_1 \\
 \varepsilon_2 - \varepsilon_1 \\
 0 \\
 \varepsilon_3 - \varepsilon_2 \\
 0 \\
 0
 \end{bmatrix} \quad (11)$$

where  $C_{i1}$ ,  $C_{i2}$  are the coefficients in section  $i$ .

The temperature distribution along the entire length of the V-beam can be used to calculate the expansion of the silicon using

$$\Delta L = 2\chi \int_0^{l+b} [T(x) - T_0] dx \quad (12)$$

where  $\chi$  is the thermal expansion coefficient of silicon, which is assumed to be approximately constant over the temperature values investigated, and a factor of two is included to account for modeling only half of the V-beam. Given the value of  $\Delta L$  from eq. (12), eq. (4) can be used to predict the change in cavity length for a given input laser power. Table 1 shows the parameters of the accelerometer and material constants used in this article. From theoretical modeling, a 30 mW incident laser power is expected to induce a 762 nm change in cavity length, which is sufficient for calibration with a wavelength of interrogation  $\leq 1524 \text{ nm}$ . The expected temperature distribution along the length of the V-beam in this case is shown in Fig. 4. The maximum temperature



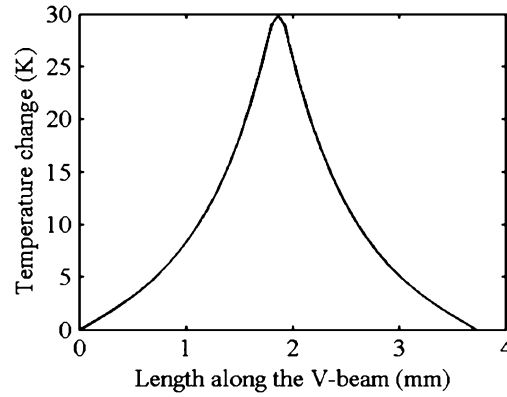


Fig. 4. Theoretical temperature distribution along the length of the V-beam for a 785 nm laser with 30 mW incident on the silicon mirror block.

change expected is no greater than 30 K, underlining the validity of neglecting radiative losses and assuming the thermal expansion coefficient of silicon is constant. The modeling also confirmed that differences in spot size only marginally affect the temperature in the irradiated region while having a negligible effect on the temperature distribution elsewhere in the structure. This is to be expected since the total input power remains constant and highly localized compared to the length of the V-beam.

### 2.3. In-Phase and Quadrature Readout

Assuming a low-finesse FPI cavity interrogated at two different wavelengths  $\lambda_1, \lambda_2$ , the intensities  $I_1, I_2$  of the returned signals will be approximately of the form [12]

$$I_1 = a_1 + b_1 \cos(\varphi_1) \quad I_2 = a_2 + b_2 \cos(\varphi_2) \quad (13)$$

where  $a_i$  are the dc components,  $b_i/a_i$  are the fringe visibilities, and  $\varphi_i$  are the round-trip phase shifts which depend on the cavity length  $l_c$  according to

$$\varphi_i = \left( \frac{2\pi}{\lambda_i} \right) 2l_c, \quad i = 1, 2. \quad (14)$$

By selecting the interrogation wavelengths such that the round-trip phase shifts differ by  $\pi/2$ , the variations of  $I_1$  and  $I_2$  with cavity length can be arranged to be in quadrature. For example, if  $\varphi_2 = \varphi_1 - \pi/2$ , eq. (13) can be re-written as

$$I_1 = a_1 + b_1 \cos(\varphi_1), \quad I_2 = a_2 + b_2 \sin(\varphi_1). \quad (15)$$

Given both of the signals  $I_1$  and  $I_2$ , it is possible to measure changes in cavity length without the ambiguities that arise from the periodic nature of the FPI output when only a single interrogation wavelength is used. In practice I&Q readout can be implemented by illuminating the FPI cavity with a broad-band source, and then splitting the return signal into two paths containing band-pass filters centered on the desired interrogation wavelengths. The purpose of the calibration procedure is to establish the values of the parameters  $a_1, b_1, a_2, b_2$ ; this involves varying the cavity length so that both outputs explore their entire ranges and the maximum and minimum values can be recorded. Once these parameters are known, the transducer signals can be normalized as  $I'_1 = (I_1 - a_1)/b_1$  and  $I'_2 = (I_2 - a_2)/b_2$  so that

$$I'_1 = \cos(\varphi_1), \quad I'_2 = \sin(\varphi_1) \Rightarrow \varphi_1 = \tan^{-1} \left( \frac{I'_2}{I'_1} \right). \quad (16)$$



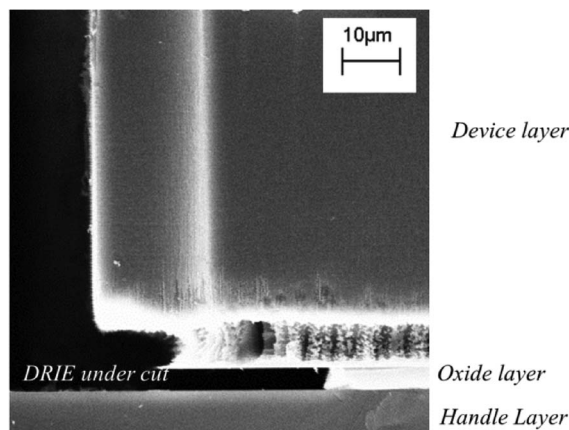


Fig. 5. SEM image showing the side view of a DRIE'd silicon structure following the HF release etch. The oxide layer has been undercut by  $\sim 30 \mu\text{m}$ , and notching is evident at the base of the silicon structure.

#### 2.4. Design Chosen for Fabrication

The target specifications in this work called for a device with a resonant frequency of 15 kHz and with the capability of photo-thermal calibration using a 785 nm laser with a maximum power of 100 mW. A hammock suspension was employed comprising six flexures, each 1.6 mm long and  $78 \mu\text{m}$  wide, in conjunction with a V-beam 1.8 mm long and  $20 \mu\text{m}$  wide with an angle of  $2^\circ$ . This design resulted in theoretical thermal and mechanical amplification factors of  $\sim 7.4$  and  $\sim 13$ , respectively. To achieve the desired resonant frequency, a proof mass with dimensions  $1.978 \times 1.978 \text{ mm}^2$  was required; these dimensions were confirmed using a Comsol eigen-frequency analysis of the whole device. A hammock suspension has the advantage that it can be made very stiff in the axes orthogonal to the intended direction of motion, minimizing cross-axis sensitivity. This comes at the expense of non-linearity under large deflections; however, this is not expected to be an issue for an FPI device since the proof mass displacements are designed to be  $< 1 \mu\text{m}$  under normal operation.

### 3. Experimental Methods

#### 3.1. Device Fabrication

Prototype accelerometers were fabricated on a BSOI wafer with an  $85 \mu\text{m}$ -thick mechanical layer, using a single mask process. The mechanical layer thickness was chosen to be  $\sim 25 \mu\text{m}$  greater than the  $62.5 \mu\text{m}$  radius of a single mode optical fiber (Corning SMF-28), so that the optical beam from the fiber impinged on the silicon sidewall near the top surface. The wafer was spin-coated with S1828 positive photoresist and exposed in a mask aligner. Development of the resist was followed by deep reactive ion etching (DRIE) of the silicon mechanical layer. After dicing of the wafer, individual dies were suspended over a pool of 40% hydrofluoric acid (HF) at a temperature of  $40^\circ\text{C}$  to allow the vapor to etch away the buried oxide layer and release the moving parts.

An SEM image of a device following HF release is shown in Fig. 5. The image clearly shows the removal of the buried oxide layer due to HF etching. Some “notching” or undercutting of the silicon is also evident in the image; this effect is frequently seen with silicon DRIE when etching down to a buried oxide layer. In this paper, the undercut was  $\sim 10 \mu\text{m}$  wide  $\times \sim 6 \mu\text{m}$  high, and because the V-beams were only  $20 \mu\text{m}$  wide this resulted in the gap  $d_b$  between the V-beam and the substrate increasing from  $4 \mu\text{m}$  (the buried oxide thickness) to  $\sim 10 \mu\text{m}$ . This was taken into account in the thermal modeling.

Following release, each device was sputter-coated with a  $\sim 200 \text{ nm}$  thick layer of gold. Gold was selected since it does not oxidize and gives the FPI mirror the maximum reflectivity possible [26],

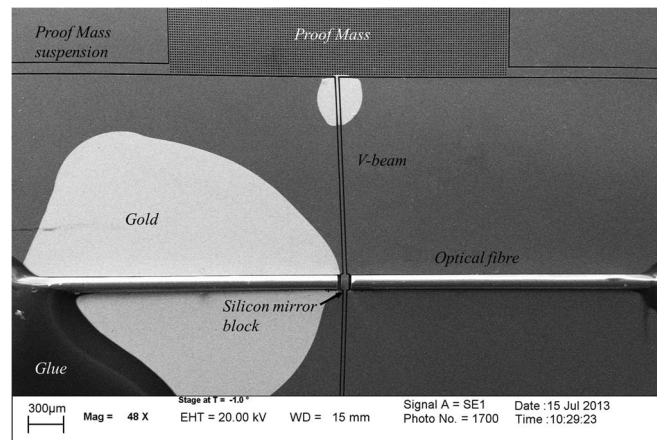


Fig. 6. SEM image of prototype device after HF release and with optical fibers glued in position.

eliminating unwanted spurious multiple cavity effects. It was necessary then to remove the gold from the opposite side of the mirror block, and this was done by selective etching. AZ9260 resist was dispensed into one of the optical fiber grooves and allowed to flow up to the mirror surface where its high viscosity meant it was unable to flow beneath or around the silicon block or V-beam. After baking the resist, the exposed gold was removed using an iodine-based gold etchant, with the AZ9260 resist protecting one side of the silicon mirror block. Finally, the resist was removed using acetone and the device was freeze dried to avoid possible stiction of the released structures.

A cleaved optical fiber was inserted into the alignment groove on the gold plated side with the aid of a microscope and a pair of 3-axis micro-positioning stages (one for the device and one for the fiber). The cleaved fiber end was positioned between 20 and 40  $\mu\text{m}$  from the mirror, so as to produce an FPI cavity with a free-spectral range between 60 nm and 30 nm at 1550 nm wavelength. This choice of FSR was compatible with the tunable filters used in the interrogation setup, and the cavity length ensured that the fiber was always at a safe distance from the mirror which was constrained to a maximum displacement of 10  $\mu\text{m}$ . The reflection spectrum of the FPI was continuously monitored during the fiber insertion process using an optical spectrum analyzer (OSA). Following alignment, the fiber was secured permanently using Loctite 358 UV curable adhesive.

Once the interrogation fiber was in place, the same procedure was used to insert a second fiber for photothermal actuation on the uncoated side of the mirror block. An SEM image of the final device, with both fibers in position, is shown in Fig. 6. There is a large gold-coated region around the left-hand optical fiber, highlighting the location of the resist used to protect one side of the mirror block during the gold etching process.

### 3.2. Calibration and Measurement of Performance

A prototype accelerometer was calibrated and tested using the setup shown in Fig. 7. Interrogation of the FPI was carried out using light from a broadband source (type Agilent 834378A), centrally located at 1550 nm. This was coupled into the device via a circulator. The light reflected from the FPI was divided into two equal components using a 3 dB coupler; these were fed to separate amplified photodiodes via a pair of tunable optical filters (Newport Corporation type TBF-1550-1.0, 20 dB bandwidth of 3.5 nm) which were set to be I&Q with reference to the FPI spectrum of the device. The photodiode outputs were recorded using a National Instruments data acquisition module which allowed sampling at up to 24 kbits/s on each channel. Analysis of the recorded data was carried out using a LabView program.

The source used for photothermal actuation was a 785 nm laser with a single-mode fiber pig-tail (Thorlabs type LP785-SF100). During the calibration process the output power of the laser was modulated over the range 0 to 30 mW while simultaneously recording the I&Q photodiode outputs. The I&Q datasets were then plotted against each other to form a Lissajous figure. Using MATLAB,

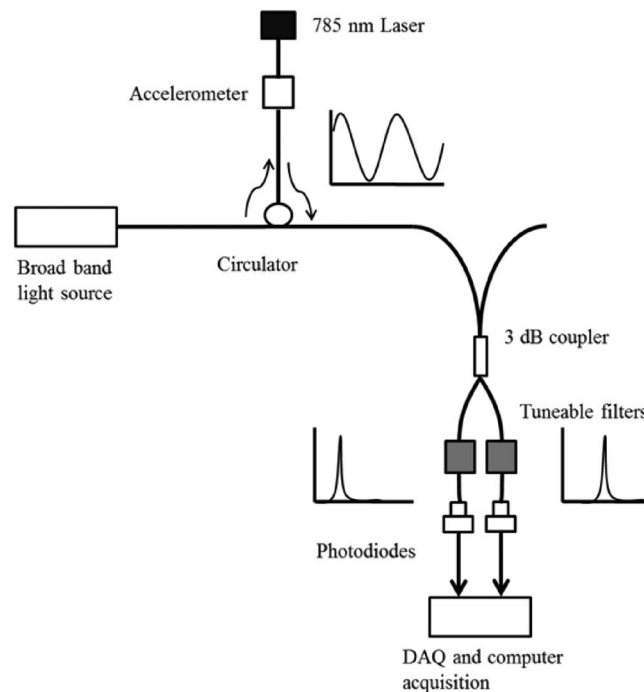


Fig. 7. Experimental setup used to investigate the performance of the accelerometer using I&Q as the interrogation technique.

an ellipse was fitted to the data using the centroid method described in [27] where the calculated parameters are of a general quadratic curve. These values were used to determine the coefficients in eq. (15).

Following calibration, the linearity of the relationship between NIR laser power and cavity length was investigated. The laser power was manually stepped from 0 to 32 mW in 2 mW increments. The reflection spectrum was recorded at each power setting using an optical spectrum analyzer. The mode order was calculated from this and combined with the measured shift in the FPI fringes to calculate the induced change in cavity length.

The performance of the device as an accelerometer was tested by mounting it on an aluminum block attached to a digitally controlled shaker table (IMV type PET-05). At a fixed frequency of 50 Hz, the shaker table was capable of producing a sinusoidal output ranging from 0.01 g to 15 g, zero-to-peak. The output acceleration of the shaker was controlled in a feedback loop using two commercial capacitive accelerometers, Analog Devices type ADXL326 (0.1 to 15 g) and ADXL335 (0 to 0.1 g), mounted immediately adjacent to the device under test. The I&Q intensities were recorded for 10 seconds at each acceleration level and converted to an equivalent variation in phase. A fast Fourier transform (FFT) was then performed on the extracted phase signal and the magnitude of the spectral peak at 50 Hz was taken as a measure of the accelerometer's response.

The noise floor was established by acquiring data with the accelerometer at rest and then converting the extracted phase signal to a power spectral density plot. This conversion was carried out using the *pcov* covariance function in MATLAB, with an order of 300 and a phase-to-acceleration conversion factor based on the accelerometer test results. For these measurements the photodiode signals were band-limited to 3 kHz using a pair of active low-pass filters.

#### 4. Experimental Results

Fig. 8 shows a typical set of data from the photothermal calibration process. Fig. 8(a) shows the raw I&Q signals from the two amplified photodiodes, plotted as a function of time as the power of the 785 nm laser is varied. The corresponding Lissajous diagram is shown in Fig. 8(b) along with the

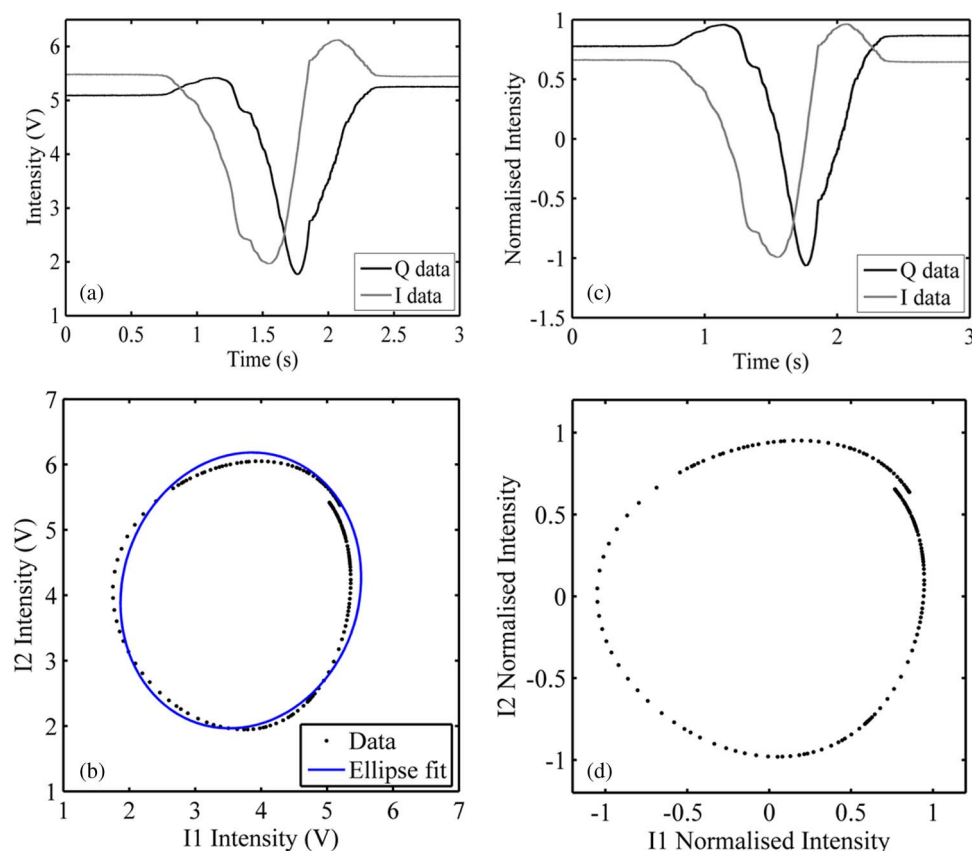


Fig. 8. Typical photothermal calibration data acquired by manually tuning the 785 nm laser power from 0 to 27.4 mW. (a) Raw I&Q photodiode signals captured during the laser intensity sweep; (b) Lissajous figure for raw I&Q signals; (c) normalized I&Q signals after correction for offset and scaling; (d) Lissajous figure for normalized I&Q signals.

best-fit ellipse which was used to estimate the parameters for normalization and removal of the dc components. The resulting normalized I&Q signals and the corresponding Lissajous diagram are shown in Fig. 8(c) and (d), respectively. According to eq. (16) the normalized Lissajous diagram should be a unit circle; however, the variations of the raw I&Q signals with the cavity length are not purely sinusoidal, and this leads to the distortions seen in Fig. 8(d). Moreover, it can be seen that the Lissajous diagram is not closed, indicating that the I&Q signals are not quite periodic with respect to changes in the cavity length. The reasons for this are not yet fully understood. The FPI response is also non-periodic with respect to changes in optical wavelength, as can be seen from the linear plot of the FPI spectrum in Fig. 9. Although the variation in the returned intensity is roughly sinusoidal, there is some modulation of both the amplitude and the dc level with wavelength.

The variation of cavity length with laser power over the range 0 to 32 mW is shown in Fig. 10, along with the linear variation predicted by the approximate 1D thermal model. The overall trend in the experimental data is in good agreement with the theoretical prediction, producing a 785 nm cavity length change at a laser power of 30 mW. The reason for the departures from linearity in the experimental data is currently unknown and will be investigated in future work, as will the extent of any hysteresis effects that might arise as a result of heat being retained in the device following photothermal calibration.

Fig. 11 shows a typical example of an extracted phase signal obtained under an applied acceleration, in this case a sinusoidal excitation of amplitude 1 g zero-to-peak at 50 Hz frequency. The performance of the device over a range of input accelerations is shown in Fig. 12. The accelerometer had a sensitivity of 0.081 rad/g and could operate down to 0.01 g and up to 15 g

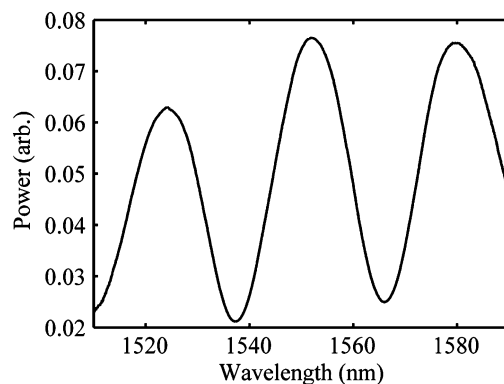


Fig. 9. FPI reflection spectrum acquired with optical spectrum analyzer and an Agilent 834378A broadband light source showing departure from the assumed sinusoidal form.

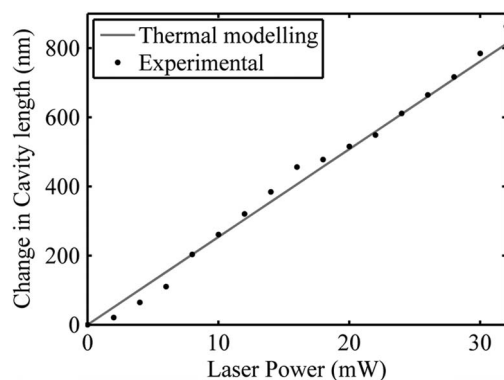


Fig. 10. Measured and theoretically predicted variations of cavity length with NIR laser power.

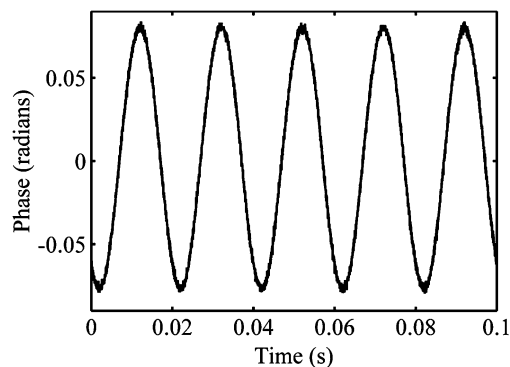


Fig. 11. Extracted phase signal obtained when the accelerometer is subject to a sinusoidal input acceleration of amplitude 1 g (zero-to-peak) at 50 Hz.

giving a dynamic range greater than  $10^3$ . The accelerations applied, which were limited in range by the reference accelerometers used, induced a maximum change in phase of 1.13 radians, so it was not possible to test the device over multiple fringes. The device showed a near linear response over the range examined, with the departures from non-linearity being attributed mainly to the non-sinusoidal FPI response. This could in principle be corrected for by using the measured Lissajous figure to map the I&Q intensities to the phase.

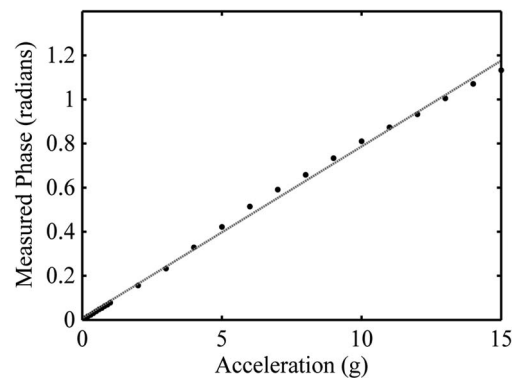


Fig. 12. Measured accelerometer response of the device for sinusoidal input accelerations in the range 0.01 to 15 g at 50 Hz, with a linear line of best fit through the data.

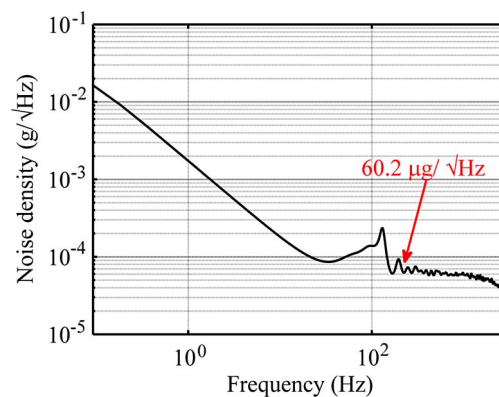


Fig. 13. Noise power spectrum at the output of the device (extracted phase signal) under zero input acceleration, plotted using MATLAB covariance function.

A power spectral density plot showing the noise spectrum at zero input acceleration is shown in Fig. 13. This plot shows the noise in the extracted phase signal, although the vertical axis has been converted into units of  $\text{g}/\sqrt{\text{Hz}}$  using the sensitivity of the device (i.e., the gradient in Fig. 12) as a conversion factor. At low frequencies, the spectrum shows the characteristic form of  $1/f$  noise, while from 100 to 3,000 Hz the noise floor of the system is approximately  $60 \mu\text{g}/\sqrt{\text{Hz}}$ . This is higher than reported for other sensors interrogated using the I&Q technique [11], [14] and could be improved through reduction of noise contributions in the readout electronics. The device is intended to operate from dc up to 3.0 kHz, and over this frequency range the limit of detection is 47.7 mg calculated using the data in Fig. 13.

## 5. Conclusion

A V-beam amplified FPI accelerometer has been presented which uses photothermal actuation for calibration of an I&Q readout system. A prototype device was fabricated with a V-beam of length 1.8 mm, width  $20 \mu\text{m}$  and angle  $2^\circ$ , giving a mechanical amplification  $\sim 13$ . A near-infrared laser (785 nm wavelength) with a power of up to 30 mW was used heat the structure, and was found to be capable of inducing a 785 nm cavity length change, sufficient for calibration of wavelengths up to 1570 nm. The accelerometer response was explored by applying 50 Hz sinusoidal input accelerations and measuring the amplitude of the extracted I&Q phase signal via a large sampled FFT. The response was found to be approximately linear, and using this narrow-band readout method accelerations over the range 0.01 to 15 g could be recorded. The real life



performance of the device was estimated using a noise spectrum and this gave a limit of detection of 47.7 mg over the intended operating bandwidth of 3 kHz.

The use of photothermal actuation allows remote calibration over optical fiber, allowing the advantages of an all-optical approach to be retained. The V-beam amplified design lends itself particularly well to this approach as the V-beam structure can be actuated directly by laser heating. Although the photothermal calibration was implemented here using separate actuation and sensing fibers on opposite sides of the device, a single fiber solution could also be envisaged. For example, a shorter wavelength laser operating in the ultra-violet region could be used to heat the gold-metallized mirror surface via the interrogation fiber. This possibility, which would simplify packaging and provide a more elegant and widely deployable solution, will be explored in future work. Fuller use of the data acquired during calibration to improve the linearity of the accelerometer response will also be investigated.

## References

- [1] T. A. Berkoff and A. D. Kersey, "Experimental demonstration of a fiber Bragg grating accelerometer," *IEEE Photon. Technol. Lett.*, vol. 8, no. 12, pp. 1677–1679, Dec. 1996.
- [2] A. Fender *et al.*, "Two-axis temperature-insensitive accelerometer based on multicore fiber Bragg gratings," *IEEE Sensors J.*, vol. 8, no. 7, pp. 1292–1298, Jul. 2008.
- [3] A. Llobera, V. Seidemann, J. A. Plaza, V. J. Cadarso, and S. Buttgenbach, "Integrated polymer optical accelerometer," *IEEE Photon. Technol. Lett.*, vol. 17, no. 6, pp. 1262–1264, Jun. 2005.
- [4] G. A. Rines, "Fiber-optic accelerometer with hydrophone applications," *Appl. Opt.*, vol. 20, no. 19, pp. 3453–3459, Oct. 1981.
- [5] T. Ke, T. Zhu, Y. Rao, and M. Deng, "Accelerometer based on all-fiber Fabry–Pérot interferometer formed by hollow-core photonic crystal fiber," *Microw. Opt. Technol. Lett.*, vol. 52, no. 11, pp. 2531–2535, Nov. 2010.
- [6] K. Zandi *et al.*, "In-plane silicon-on-insulator optical MEMS accelerometer using waveguide Fabry–Pérot microcavity with silicon/air Bragg mirrors," in *Proc. 23rd IEEE Int. Conf. MEMS*, 2010, pp. 839–842.
- [7] M. D. Pocha, G. A. Meyer, C. F. McConaghy, S. P. Swierkowski, and J. D. Wolfe, "Miniature accelerometer and multichannel signal processor for fiber optic Fabry–Pérot sensing," *IEEE Sensors J.*, vol. 7, no. 2, pp. 285–292, Feb. 2007.
- [8] M. A. Perez and A. M. Shkel, "Design and demonstration of a bulk micromachined Fabry–Pérot  $\mu$ g-resolution accelerometer," *IEEE Sensors J.*, vol. 7, no. 12, pp. 1653–1662, Dec. 2007.
- [9] A. Ya'akovovitz and S. Krylov, "Toward sensitivity enhancement of MEMS accelerometers using mechanical amplification mechanism," *IEEE Sensors J.*, vol. 10, no. 8, pp. 1311–1319, Aug. 2010.
- [10] I. Zeimpekis, I. Sari, and M. Kraft, "Characterization of a mechanical motion amplifier applied to a MEMS accelerometer," *J. Microelectromech. Syst.*, vol. 21, no. 5, pp. 1032–1042, Oct. 2012.
- [11] A. Ezbi and R. P. Tatam, "Passive signal processing for a miniature Fabry–Pérot interferometric sensor with a multimode laser-diode source," *Opt. Lett.*, vol. 20, no. 17, pp. 1818–1820, Sep. 1995.
- [12] P. G. Jia and D. H. Wang, "Self-calibrated non-contact fibre-optic Fabry–Pérot interferometric vibration displacement sensor system using laser emission frequency modulated phase generated carrier demodulation scheme," *Meas. Sci. Technol.*, vol. 23, no. 11, p. 115 201, Nov. 2012.
- [13] Y. G. Lee, D. H. Kim, and C. G. Kim, "Performance of a single reflective grating-based fiber optic accelerometer," *Meas. Sci. Technol.*, vol. 23, no. 4, p. 045101, Apr. 2012.
- [14] Y. L. Lo, J. S. Sirkis, and C. C. Chang, "Passive signal processing of in-line fiber etalon sensors for high strain-rate loading," *J. Lightwave Technol.*, vol. 15, no. 8, pp. 1578–1586, Aug. 1997.
- [15] Y. L. Lo and J. S. Sirkis, "Passive demodulation techniques for Michelson and polarimetric optical fiber sensors," *Exp. Tech.*, vol. 19, no. 3, pp. 23–27, May 1995.
- [16] T. Požar and J. Možina, "Enhanced ellipse fitting in a two-detector homodyne quadrature laser interferometer," *Meas. Sci. Technol.*, vol. 22, no. 8, p. 085301, Aug. 2011.
- [17] E. Davies, D. S. George, M. C. Gower, and A. S. Holmes, "Optical accelerometer with mechanical amplification via a V-beam mechanism," in *Proc. IEEE 26th Int. Conf. MEMS*, Taipei, Taiwan, 2013, pp. 609–612.
- [18] E. Davies, D. S. George, M. C. Gower, and A. S. Holmes, "MEMS Fabry–Pérot optical accelerometer employing mechanical amplification via a V-beam structure," *Sens. Actuators A, Phys.*, Aug. 2013, to be published. [Online]. Available: <http://dx.doi.org/10.1016/j.sna.2013.08.002>
- [19] L. M. Zhang, D. Uttamchandani, and B. Culshaw, "Measurement of the mechanical properties of silicon microresonators," *Sens. Actuators A, Phys.*, vol. 29, no. 1, pp. 79–84, Sep. 1991.
- [20] A. V. Churenkov, "Photothermal excitation and self-excitation of silicon microresonators," *Sens. Actuators A, Phys.*, vol. 39, no. 2, pp. 141–148, Nov. 1993.
- [21] L. Ma, D. Zhang, C. Liu, and H. Zhang, "Theoretical modelling and experimental study of novel photothermal microactuators," *Chin. Opt. Lett.*, vol. 7, no. 8, pp. 694–698, Aug. 2009.
- [22] C. Liu, Y. He, H. Zhang, and D. Zhang, "Analysis and experimentation of novel asymmetric photo-thermal micro-actuator," in *Proc. 4th Int. Symp. Precision Mech. Meas.*, 2008, pp. 713011-1–713011-6.
- [23] F. R. Szabo and P. E. Kladitis, "Design, modeling and testing of polysilicon optothermal actuators for power scavenging wireless microrobots," in *Proc. ICMENS*, 2004, pp. 446–452.



- [24] M. R. Pac and D. O. Popa, "3-DOF untethered microrobot powered by a single laser beam based on differential thermal dynamics," in *Proc. IEEE ICRA*, 2011, pp. 121–127.
- [25] N. D. Mankame and G. K. Ananthasuresh, "Comprehensive thermal modelling and characterization of an electro-thermal-compliant microactuator," *J. Micromech. Microeng.*, vol. 11, no. 5, pp. 452–462, Sep. 2001.
- [26] C. Marxer *et al.*, "Vertical mirrors fabricated by deep reactive ion etching for fiber-optic switching applications," *J. Microelectromech. Syst.*, vol. 6, no. 3, pp. 277–285, Sep. 1997.
- [27] G. Taubin, "Estimation of planar curves, surfaces, nonplanar space curves defined by implicit equations with applications to edge and range image segmentation," *IEEE Trans. Pattern Anal. Mach. Intell.*, vol. 13, no. 11, pp. 1115–1138, Nov. 1991.